

3D MAGNETIC FIELD CONFIGURATION OF THE 2006 DECEMBER 13 FLARE EXTRAPOLATED WITH THE OPTIMIZATION METHOD

Y. GUO AND M. D. DING

Department of Astronomy, Nanjing University, Nanjing 210093, China; dmd@nju.edu.cn

T. WIEGELMANN

Max-Planck-Institut für Sonnensystemforschung, Max-Planck-Strasse 2, 37191 Katlenburg-Lindau, Germany; wiegelmann@mps.mpg.de

AND

H. LI

Purple Mountain Observatory, 2 West Beijing Road, Nanjing 210008, China

Received 2007 November 9; accepted 2008 February 18

ABSTRACT

The photospheric vector magnetic field of the active region NOAA 10930 was obtained with the Solar Optical Telescope (SOT) on board the *Hinode* satellite with a very high spatial resolution (about $0.3''$). Observations of the two-ribbon flare on 2006 December 13 in this active region provide us a good sample to study the magnetic field configuration related to the occurrence of the flare. Using the optimization method for nonlinear force-free field (NLFFF) extrapolation proposed by Wheatland et al. and recently developed by Wiegelmann, we derive the three-dimensional (3D) vector magnetic field configuration associated with this flare. The general topology can be described as a highly sheared core field and a quasi-potential envelope arch field. The core field clearly shows some dips supposed to sustain a filament. Free energy release in the flare, calculated by subtracting the energy contained in the NLFFF and the corresponding potential field, is 2.4×10^{31} ergs, which is $\sim 2\%$ of the preflare potential field energy. We also calculate the shear angles, defined as the angles between the NLFFF and potential field, and find that they become larger at some particular sites in the lower atmosphere, while they become significantly smaller in most places, implying that the whole configuration gets closer to the potential field after the flare. The Ca II H line images obtained with the Broadband Filter Imager (BFI) of the SOT and the 1600 \AA images with the *Transition Region and Coronal Explorer* (TRACE) show that the preflare heating occurs mainly in the core field. These results provide evidence in support of the tether-cutting model of solar flares.

Subject headings: Sun: flares — Sun: magnetic fields

Online material: color figures

1. INTRODUCTION

The magnetic field configuration is essential for us to understand the solar explosive phenomena, such as flares and coronal mass ejections (CMEs). By examining the coronal X-ray structure before eruptive events observed by the *Yohkoh* soft X-ray telescope (SXT; Tsuneta et al. 1991), Moore et al. (1997, 2001) depicted the field configuration associated with two-ribbon flares and CMEs. The 3D field configuration before flares can be divided into two parts, an envelope field and a core field. This division is arbitrary because the boundary between them is never so sharp. The core field is highly sheared and twisted, while the envelope field straddling above the core field is less sheared. The SXT observations revealed that the core field has a sigmoidal structure (Rust & Kumar 1996; Sterling & Hudson 1997; Moore et al. 1997, 2001). This fact was also observed in EUV wavelengths (Liu et al. 2007). The S-shaped or reverse S-shaped structure traces the sheared and twisted core field lines, and the ends of the field lines are rooted in the opposite-polarity zones. The envelope field is archlike and strides over the polarity inversion line and the core field. The footpoints of the envelope field in the photosphere are more distant from the inversion line than those of the core field.

Based on observations and theoretical studies, Hirayama (1974) proposed an inverted Y model for the eruptive events, which was modified by Moore & LaBonte (1980) and elaborated by Moore et al. (2001) recently. Before the explosion, the field configura-

tion consists of an envelope and a core field as described above. When the sheared core field begins to reconnect, the twisted flux rope erupts and the denser chromospheric material or the filament rises. This eruption process is explosive. During the eruption, the closed arcade envelope field is opened and stretched, so that the legs of the envelope field get close and reconnect. The lower part of the re-closed envelope field forms the postflare arcade, and the upper part is blown out to form the CME. This is the standard tether-cutting model for the eruptive events. There are also, however, many flares without filaments or CMEs.

An X3.4 flare occurred on 2006 December 13 in the active region NOAA 10930. It gives us a good sample to study the magnetic configuration and reexamine the tether-cutting model. By analyzing the data obtained with the Michelson Doppler Imager (MDI; Scherrer et al. 1995) and the *Transition Region and Coronal Explorer* (TRACE; Handy et al. 1999), Zhang et al. (2007) showed the following characteristics for this active region: development of magnetic shear, appearance of ephemeral regions, and fast rotation of a sunspot. This region has also been observed by the Solar Optical Telescope (SOT; Tsuneta et al. 2008; Suematsu et al. 2008; Ichimoto et al. 2008; Shimizu et al. 2008) on board *Hinode* (Kosugi et al. 2007). The data from *Hinode*, with a high spatial resolution and high cadence, show us a detailed temporal change of the active region (Kubo et al. 2007). The two umbrae of positive and negative polarities collided with each other within the interval of about 7 days, during which small flux regions emerged and merged. The polarity inversion line became tortuous

and complicated. After the major flare, these features disappeared or became less obvious, and the polarity inversion line appeared smoother and flatter. A careful examination of the vector magnetic field observed by the spectropolarimetry (SP) manifests the change of field directions before and after the flare.

Based on the high spatial resolution observation of the full polarization parameters (I , Q , U , and V) by the SOT/SP, we can derive the photospheric vector field through the inversion of Stokes profiles (Unno 1956; Stenflo 1985; Lites et al. 1988) and after removing the 180° ambiguity of the transverse field component (Metcalf 1994; Metcalf et al. 2006). After that, we consider deriving the 3D vector field from the 2D vector field. There are some extrapolation methods that aim to recover the coronal magnetic field (Amari et al. 1997; McClymont et al. 1997; Wiegmann 2008). In the corona we adopt the force-free assumption that $\beta = 2\mu_0 p/B^2 \ll 1$, where p is the plasma pressure and $B^2/(2\mu_0)$ is the magnetic pressure. A force-free field is described by the following equations:

$$\nabla \times \mathbf{B} = \alpha \mathbf{B}, \quad (1)$$

$$\nabla \cdot \mathbf{B} = 0, \quad (2)$$

where α is the force-free function. The relation $\alpha = 0$ corresponds to a potential field, and $\alpha = \text{const.}$ refers to a linear force-free field. In this work we consider the more sophisticated nonlinear force-free field in which α varies with space. We adopt the optimization method developed by Wheatland et al. (2000) and Wiegmann (2004). Quite recently, Schrijver et al. (2008) computed 14 different NLFFF models with four codes and different boundary conditions for the same active region. They found that preprocessing and smoothing of the bottom boundary data are necessary to derive reasonable results. The energy release related to the 2006 December 13 flare was computed to be $\sim 10^{32}$ ergs.

Taking advantage of the high-resolution data from *Hinode* and *TRACE*, and the robust optimization extrapolation method, we study the change of the 3D field configuration related to the occurrence of the X3.4 flare. The results are then used to check in particular the tether-cutting model. We describe the observations and the optimization method in §§ 2 and 3, respectively. The results are presented in § 4, while in § 5 we give our discussions and draw our conclusions.

2. OBSERVATIONS AND DATA REDUCTION

The SOT/SP on board *Hinode* obtained the line profiles of two magnetically sensitive Fe lines at 6301.5 and 6302.5 Å and the continuum nearby. The total spectral coverage is from 6300.8 to 6303.2 Å, and the spectral resolution is 30 mÅ with wavelength sampling of 21.6 mÅ. The I , Q , U , and V parameters are obtained by adding and subtracting the raw spectra. We use a nonlinear least-square fitting procedure to fit the Stokes profiles based on the Milne-Eddington model (T. Yokoyama et al. 2008, in preparation; Kubo et al. 2007), which yields the intrinsic strength of the field, B , the filling factor, f , the inclination with respect to the line of sight, γ , and the azimuth angle, θ . The line-of-sight component of the field is obtained by $B_z = Bf \cos \gamma$, and the transverse component is defined as $B_x = Bf \sin \gamma \cos \theta$ and $B_y = Bf \sin \gamma \sin \theta$. The 180° ambiguity of the azimuth angle is removed with the acute angle method (Wang 1997; Wang et al. 2001; Metcalf et al. 2006). We compare the observed field to the extrapolated linear force-free field by requiring that $-90^\circ \leq \Delta\theta \leq 90^\circ$, where $\Delta\theta$ is the angle between the observed transverse and extrapolated transverse components. Note that the reference linear force-free field is extrapolated by using the Fourier trans-

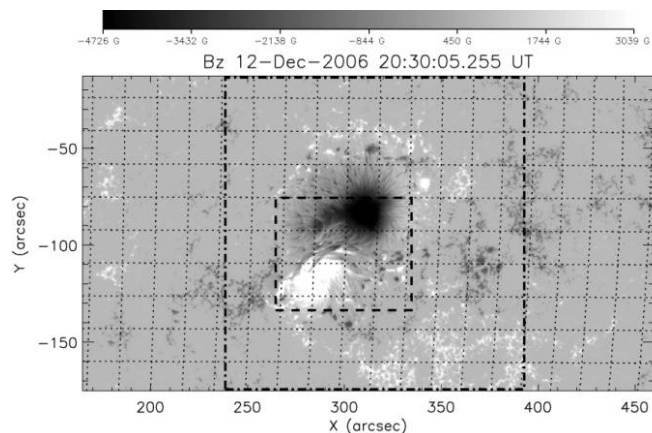


FIG. 1.—Line-of-sight magnetic field for NOAA 10930. Observation time is from 20:30 to 21:33 UT on 2006 December 12. North is up and west is to the right. White (black) pixels refer to positive (negative) polarity. The spatial resolution is about $0.3''$. The dotted lines are longitude and latitude grids. The dash-dotted rectangle marks the FOV used for the extrapolations (as shown in Fig. 2). The dashed rectangle marks the FOV for the *TRACE* and SOT/BFI images (as shown in Fig. 7).

form method with the line-of-sight field B_z as the boundary condition.

The field of view (FOV) along the slit is $164''$, and the slit width is $0.16''$. In the fast map mode, the spatial sampling is $0.295'' \times 0.317''$ and the time cadence is 3.2 s. Scanning perpendicular to the slit direction makes an observation of an area within a range of $\pm 164''$. Figure 1 shows the latest observation of the line-of-sight magnetic field before the X3.4 flare. This active region is located in the southwestern part of the solar disk. The FOV that we select to make extrapolation is $164'' \times 164''$ centered at the midpoint of the scanning, which means that we use all the data points along the south-north direction but half of the points along the east-west direction.

The Broadband Filter Imager (BFI) observed Ca II H 3968.5 Å images with a time cadence of 2 minutes and a space sampling of $0.108''$. The FOV is $218'' \times 109''$, which is smaller than that of SP. The Ca II H line is sensitive to temperature of $\sim 10^4$ K, thereby it is used to study the chromospheric heating. We also use the *TRACE* 1600 Å images with $0.5''$ pixel resolution, which provide information of the heating in the upper chromosphere and the transition region.

3. THE EXTRAPOLATION METHOD

We choose the NLFFF extrapolation method to reconstruct the 3D coronal field. The force-free field obeys equations (1) and (2). Note that the potential field and the linear force-free field cases do not apply to active regions, in particular flare-producing regions, in which nonlinearity of the α -parameter dominates. Schrijver et al. (2005) showed that nonpotentiality of the active region field occurs when a new flux emerges, or when rapidly evolving opposite-polarity regions are in contact, which is rather similar to this case that we study. In addition, Régnier et al. (2002) found that the force-free function α usually changes in space. A comparison of potential, linear, and nonlinear force-free field models with directly observed 3D magnetic loops (Wiegmann et al. 2005b) and with H α images (Wiegmann et al. 2005a) revealed that nonlinear models are necessary for an accurate magnetic field reconstruction. Therefore, potential and linear force-free fields are not adequate and underestimate the free energy residing in the magnetic fields in the active region.

Several numerical methods of the nonlinear force-free field extrapolation have been developed so far, such as the Grad-Rubin-based method, Greens function-like method, magnetofrictional (MHD relaxation) method, optimization method, and upward integration method (Wiegmann 2008). Schrijver et al. (2006) made a blind test of the six algorithms based on the above methods (except for upward integration method) and compared the result with analytical solutions. They found that the optimization method proposed by Wheatland et al. (2000) and coded by Wiegmann (2004) is the fastest converging and best-performing algorithm.

Wiegmann (2004) introduced a weighting function in the optimization method. The approach is to minimize the objective function,

$$L = \int_V \omega(x, y, z) \left[B^{-2} |(\nabla \times \mathbf{B}) \times \mathbf{B}|^2 + |\nabla \cdot \mathbf{B}|^2 \right] dV, \quad (3)$$

where $\omega(x, y, z)$ is the weighting function. Without the weighting function ($\omega = 1$), this method is reduced to the case proposed by Wheatland et al. (2000). In practice, to recover the coronal field, only bottom boundary conditions are available. Thereby, we use the potential extrapolation of the line-of-sight field at the bottom boundary to get the values at the side and top boundaries. In addition, we introduce the weighing function to minimize the side and top boundary effects.

According to the code test by Metcalf et al. (2008), when the codes are applied to the forced photospheric boundary data, the reference field is not well recovered. But preprocessing of the photospheric data improves the result. In fact, the photospheric boundary data are usually noisy and not consistent with the assumption of a force-free field. Therefore, such data should be preprocessed to agree with Aly's criteria (1989) and the smoothness condition before we perform the extrapolation. Such a preprocessing routine has been developed by Wiegmann et al. (2006). In this paper we take advantage of the routine to preprocess the observed photospheric boundary data before the extrapolations.

4. DATA ANALYSIS AND RESULTS

4.1. Magnetic Configurations

Based on the optimization method, we use the vector field observed by SOT/SP to compute the 3D vector field (B_x, B_y, B_z) in a box of $128 \times 128 \times 128$ grids. Magnetic field lines are defined as

$$d\mathbf{r} \times \mathbf{B} = 0, \quad (4)$$

where $d\mathbf{r} = (dx, dy, dz)$. Equation (4) can also be written as follows for convenience of numerical integration:

$$\frac{dx}{B_x} = \frac{dy}{B_y} = \frac{dz}{B_z} = \frac{ds}{\sqrt{B_x^2 + B_y^2 + B_z^2}}. \quad (5)$$

We plot the field lines in Figure 2, where the top rows are extrapolations from the data observed from 20:45 to 21:15 UT on 2006 December 12 and the bottom ones are the results from the data observed from 04:45 to 05:15 UT on 2006 December 13. For the sake of revealing the topological and geometrical features clearly, we denote the field lines with different colors. Blue, red, and black lines represent the three line systems of different connections, which may play different roles in this two-ribbon flare. The main features of the results are described as follows:

1. Basically, the field lines are divided into two parts: the core field, which is low lying (*denoted by blue color*), and the enve-

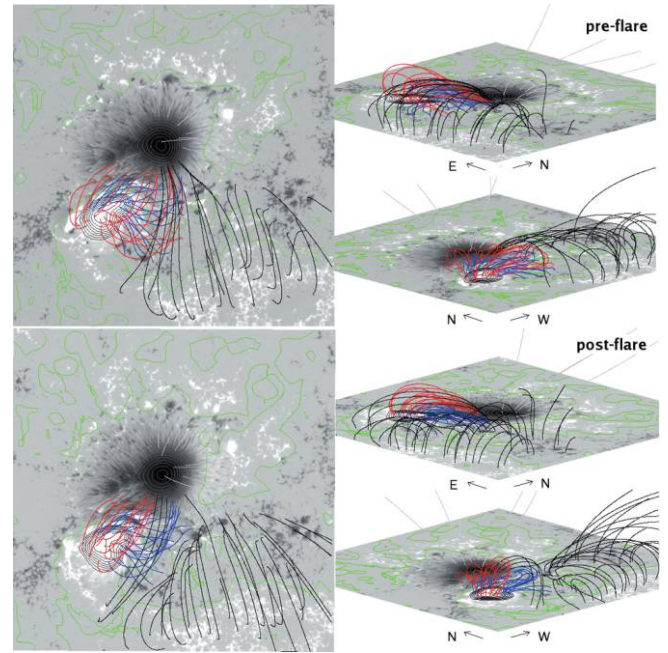


FIG. 2.—Extrapolated 3D magnetic field at a preflare time (*top row*; 20:45–21:15 UT, 2006 December 12) and a postflare time (*bottom row*; 04:45–05:15 UT, 2006 December 13). The left images are for top view, while the right images are for side view with different angles. The gray-scale images correspond to the line-of-sight field overlaid with contour levels. The polarity inversion line is denoted by the green color. See text for details about the field lines.

lope field, which is high lying (*denoted by red and black colors*). The envelope field can further be divided into two parts: the lower envelope field (*red*), rooted on the concentrated positive polarity and connected to the dispersive opposite polarity, and the higher envelope field (*black*), striding over the polarity inversion line and forming a long arcade. We term the surface between the core field and the lower envelope field the lower interface and that between the lower envelope field and the higher envelope field the upper interface.

2. The core field is highly twisted and sheared before the flare. The angle between the field line and the polarity inversion line can be less than 20° . The height of the field is down to thousands of kilometers and even to the chromospheric level. After the explosion, the core field evolves towards the potential field, but some nonpotentiality still exists. Especially, the nearer the footpoint is to the polarity inversion line, the more highly sheared the field line is.

3. Before the explosion, the lower envelope field is $\sim 1 \times 10^4$ km high, and the higher one is up to $\sim 2 \times 10^4$ km high. These field lines are nearly perpendicular to the polarity inversion line, which shows that they are less twisted and sheared and close to a potential field. After the explosion, the higher envelope field can be as high as 3×10^4 km, while the potentiality of the field remains.

4. We do not find clear evidence showing the sigmoid features in this extrapolation. As Moore et al. (2001) showed, a sigmoid has an oppositely curved elbow on each end, which extends out of the envelope field. Opposite to the extended elbow structures of the sigmoid, the core field in this case is only twisted and sheared and totally wrapped by the lower envelope field.

5. We find dips in the preflare core field as shown in Figure 3 (*top row*). Basically, the dips are distributed along the polarity inversion line. The dips are supposed to sustain a filament that has been observed by the $H\alpha$ spectroheliograph at the Paris-Meudon

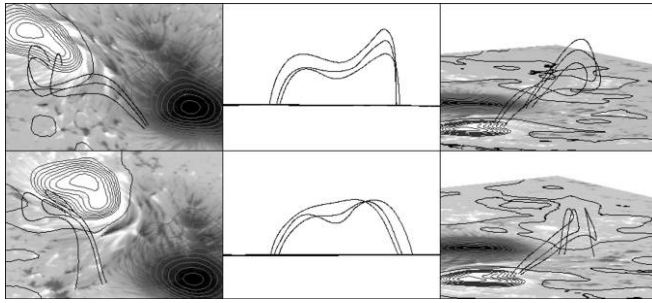


FIG. 3.—Magnetic field lines showing dips in the core field before the flare (*top row*) and after the flare (*bottom row*). The left column is for side view from west to east, the middle column for edge-on view from south to north, and the right column for side view from southeast to northwest on the solar surface. To reveal the dip feature clearly, we arbitrarily enlarge the vertical size by 4 times. [See the electronic edition of the Journal for a color version of this figure.]

observatory. From the top left panel of Figure 3 we find that the twist of the field lines is about one turn. These features can still be found after the explosion.

4.2. Magnetic Energy Release

In addition to the data observed on 2006 December 12 (20:45–21:15 UT) and on December 13 (04:45–05:15 UT), we select more data to calculate the magnetic energy and check its evolution. The two more time periods are 04:05–04:35 and 15:45–16:15 UT on December 12. The magnetic energy is defined as

$$E_m = \int_V \frac{B^2}{8\pi} dV. \quad (6)$$

The free energy of the NLFFF is then defined as

$$\Delta E_m = E_m^{\text{nlfff}} - E_m^{\text{pot}}, \quad (7)$$

where E_m^{nlfff} and E_m^{pot} are the magnetic energies of the NLFFF and the potential field, respectively. The potential field holds a minimum energy for a given line-of-sight photospheric magnetic field. An estimate of the free energy defined above is helpful to understand the energy release in the eruptive phenomena.

The results of magnetic field energy are listed in Table 1. The release of free energy during the X3.4 flare is about 2.4×10^{31} ergs, about 2% of the potential field energy at 20:45–21:15 UT. The free energy released is 1 order of magnitude smaller than the results of Schrijver et al. (2008). The change of free energy held in the NLFFF is displayed in Figure 4, where the flare duration is also marked. We find that the energy release occurs continually throughout the evolution of the magnetic field, while it is explosive during the occurrence of the flare and CME. After the explosion, the free energy is not released completely. There is

still some free energy left. Schrijver et al. (2008) also derived the free energy using different codes. In particular, when using the algorithm of Wiegmann (2004) with preprocessing and smoothing, the energy seems to increase after the flare. The reason is that they incorporated a potential transversal field to enlarge the FOV of the SOT/SP data. This assumption leads to a discontinuity of the α value that is zero in the potential field but obviously nonzero in the SOT/SP field. In fact, if using the current-field interaction method by Wheatland (2006, 2007), the energy is indeed seen to decrease after the flare (Schrijver et al. 2008).

To show if our results are quantitatively reliable, we check the degree of convergence to a force-free and divergence-free state for the extrapolated fields. We define the integral of the Lorentz force and the magnetic field divergence as (Schrijver et al. 2006):

$$L_f = \frac{1}{V} \int_V B^{-2} |(\nabla \times \mathbf{B}) \times \mathbf{B}|^2 dV, \quad (8)$$

$$L_d = \frac{1}{V} \int_V |\nabla \cdot \mathbf{B}|^2 dV. \quad (9)$$

The magnetic field and length are in units of Gauss and Mm, respectively. We list the results in Table 1. Both the values of L_f and L_d converge to a reasonably low value, although they are higher than that calculated in cases using analytical models as boundaries (Schrijver et al. 2006). This may be caused by the noise in the real measurements and the complexity of this active region. In the last column of Table 1, we also show the divergence-free measure for the corresponding potential field, L_d^{pot} , for comparison.

We also need to estimate the uncertainties of the free energies. To this end, we adopt a Monte Carlo method. As described in Tsuneta et al. (2008), the sensitivity of the SP is 1–5 G in the line-of-sight direction and 30–50 G in the transverse direction. We take the maximum value, say, 5 G for B_z and 50 G for B_x and B_y , as the standard deviations of the boundary uncertainties. First, we generate three series of pseudorandom numbers in normal distribution as the artificial errors for B_x , B_y , and B_z . The standard deviation of random errors is 5 G for B_z , and 50 G for B_x and B_y , as described above. Then we superimpose the artificial errors to the observed magnetic field and redo the 180° ambiguity removal the preprocessing and smoothing and the extrapolation. The same process is repeated 10 times for each of the four observing intervals. Finally, we calculate the standard deviations of the free energy that is also shown in Figure 4. The standard errors are found to be within 8% of the free energy. In particular, we increase the number of simulations to 30 for the time interval 20:45–21:15 UT in order to check its effect on the results. We find that the standard error changes slightly from 0.0058 to 0.0060 (normalized to the preflare potential field energy, 1.2×10^{33} ergs). The difference is within $\sim 3.3\%$.

Taylor (1974) showed that the minimum magnetic energy state is a linear (constant- α) force-free field for a given magnetic

TABLE 1
POTENTIAL FIELD ENERGY, NLFFF ENERGY, FREE ENERGY, FORCE-FREE MEASURE, AND DIVERGENCE-FREE MEASURE

Date	Time (UT)	E_m^{pot} (1.2×10^{33} ergs) ^a	E_m^{nlfff} (1.2×10^{33} ergs) ^a	ΔE_m (1.2×10^{33} ergs) ^a	L_f ($\text{G}^2 \text{Mm}^{-2}$)	L_d ($\text{G}^2 \text{Mm}^{-2}$)	L_d^{pot} ($\text{G}^2 \text{Mm}^{-2}$)
2006 Dec 12	04:05–04:35	1.11	1.25	0.14	2.01	0.92	0.14
2006 Dec 12	15:45–16:15	1.05	1.19	0.14	2.04	1.03	0.13
2006 Dec 12	20:45–21:15	1	1.11	0.11	2.27	1.15	0.13
2006 Dec 13	04:45–05:15	0.97	1.06	0.09	2.68	1.25	0.14

^a This is the potential field energy at 20:45–21:15 UT on 2006 December 12.

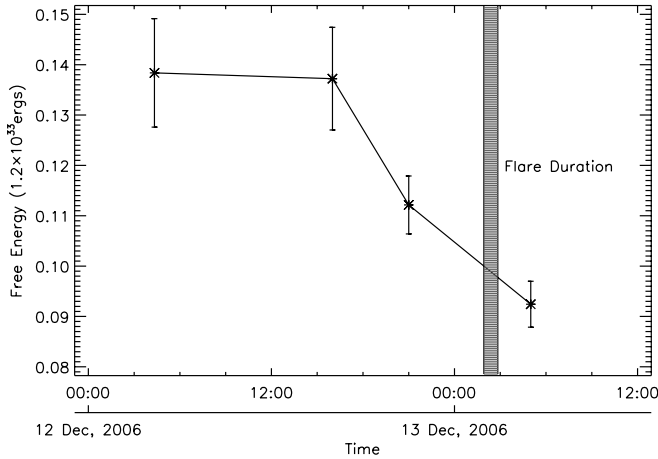


FIG. 4.—Temporal change of free energy in the NLFFF. The flare time is denoted by a vertical bar. The plotted free magnetic energy is normalized by the energy of the potential field before the flare (1.2×10^{33} ergs). The error bars show the uncertainties of the free energies.

helicity, which is conserved in ideal MHD and approximately conserved during reconnection (Berger 1998). Therefore, the free energy ΔE_m calculated here is regarded as an upper limit of the energy released during the flare.

4.3. Shear Angle Changes

We select the data observed on 2006 December 12 (20:45–21:15 UT) and on December 13 (04:45–05:15 UT) to calculate the shear angle θ , which is defined as

$$\cos \theta = \frac{\mathbf{B}_{\text{pot}} \cdot \mathbf{B}_{\text{nlfff}}}{|\mathbf{B}_{\text{pot}}| |\mathbf{B}_{\text{nlfff}}|}. \quad (10)$$

The parameter \mathbf{B}_{pot} is the potential field extrapolated with the line-of-sight magnetic field, and $\mathbf{B}_{\text{nlfff}}$ is the NLFFF extrapolated with both the line-of-sight and the transverse components (Wiegmann 2004). We calculate the shear angle θ at some selected points. These points are projected along the polarity inversion line before the flare as shown in Figure 5, but at different altitudes. And the corresponding sample points removing the effect of solar rotation after the flare are also marked in Figure 5. These points are geometrically fixed. Note that after the flare, the corresponding points may deviate slightly from the polarity inversion line that underwent some deformation during the flare.

Figure 6 plots the shear angles at different heights, which reveals the following facts. First, the maximum shear angle before the flare is about 93° , and it is about 100° after the flare, both of which appear in a shallow layer close to the photosphere. Second, the shear angles become smaller when the altitude gets higher. This means that the field is less deviated from the potential field at high altitude. Third, the shear angle before the flare is larger than that after the flare, except for the shallow layer mentioned above. In this special layer the maximum shear angle increases by $\sim 53^\circ$. This may be caused by the rotation of the sunspot, the new emerging flux, or magnetic field reconnection related to the flare. Besides this, the shear angle throughout the active region decreases significantly. This is similar to the results of Li et al. (2000), who found that the average shear of the flares associated with high shear decreases after the flares. We estimate the uncertainties in the shear angles using the same method as that for the free energy described in § 4.2. The error bars plotted in Figure 6

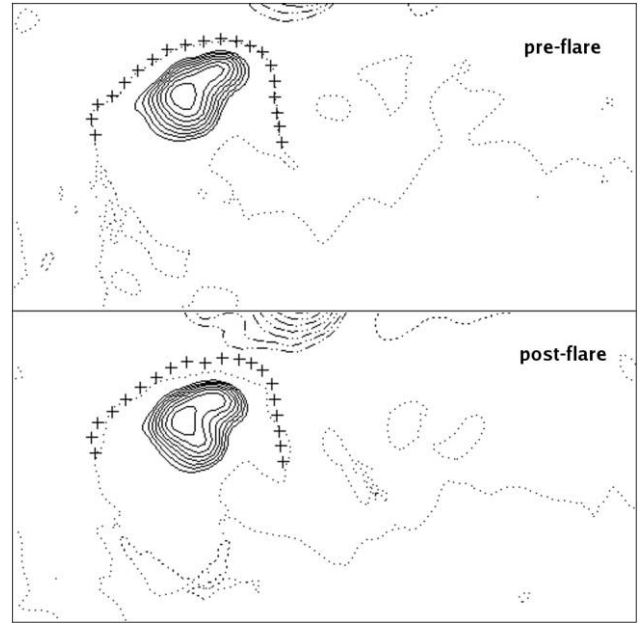


FIG. 5.—Positions of the sample points (numbered 1–20 from left to right) projected on the photosphere selected to calculate the shear angles. The top and bottom panels show the contours of photospheric magnetic field before and after the flare, respectively. The dotted line is the polarity inversion line.

show that the calculated shear angles in the central region of the core field are reliable.

4.4. TRACE 1600 Å and Ca II H 3968.5 Å Images

The TRACE 1600 Å images observed before the 2006 December 13 X3.4 flare are plotted in Figure 7 (top row). These images show the UV brightening lines in the preflare phase. The UV emission, containing contributions from UV continuum, C I and Fe II, is sensitive to temperatures of $(4.0\text{--}10.0) \times 10^3$ K. It originates from the chromosphere and the transition region—relatively low atmospheric levels. The brightening area is mainly between the two sunspots and along the polarity inversion line. Considering the 3D magnetic configuration analyzed in § 4.1, we judge that the preflare heating took place in the core field first.

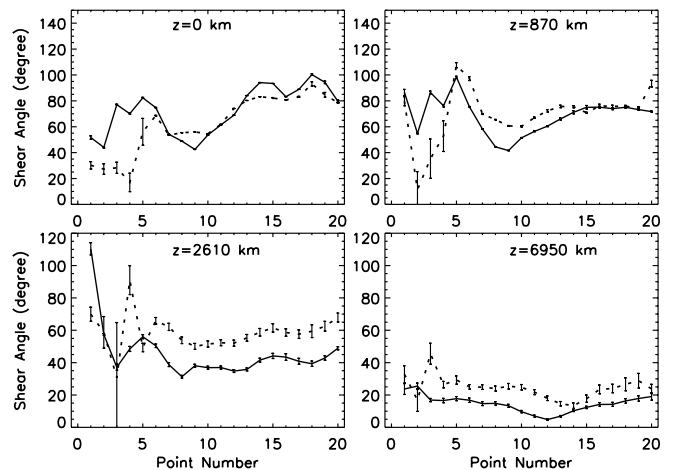


FIG. 6.—Shear angles at the sample points (Fig. 5) with different altitudes. The dotted line represents the shear angle before the flare, and the solid line represents that after the flare. The error bars show the uncertainties in the shear angles.

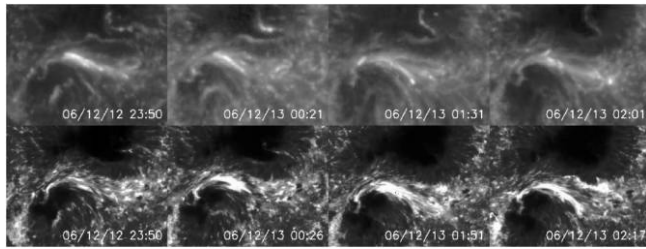


FIG. 7.— *Top*: TRACE 1600 Å images before the December 13 flare. *Bottom*: Ca II H images observed by the SOT/BFI. All the images are in a FOV of $80'' \times 60''$ centered at the heating area. North is up and west is to the right. The main heating area is between the two sunspots nearly along the polarity inversion line. [See the electronic edition of the Journal for a color version of this figure.]

The Ca II H images are also displayed in Figure 7 (*bottom row*). The Ca II H line is sensitive to temperatures of 10^4 K, which can reflect the chromospheric heating. About 2 hr before the flare onset (*bottom left*), the bright loops seen in the Ca II H images were along the highly sheared core field lines, almost parallel to the polarity inversion line. During the evolution of the magnetic field (e.g., Kubo et al. 2007), the plasma in this core field region brightened up intermittently. During the onset of the flare (*bottom right*), the two flare ribbons were first formed on both sides of, but nearly parallel to, the polarity inversion line in the core field area.

5. DISCUSSION AND CONCLUSIONS

Based on the 3D magnetic configurations before and after the flare eruption, and the heating pattern in the core field region, we find that the 2006 December 13 flare can be explained in terms of the tether-cutting model proposed by Moore & LaBonte (1980) and Moore et al. (2001). Before the explosion, the sheared and twisted core field lines lie almost horizontally under the lower envelope field. The core field lines form some dips to sustain the active region filament, which is tortuous and discontinuous and seems to pass through both the lower and higher envelope field.

The core field lines begin to reconnect because of photospheric motion (such as sunspot rotation) and/or emerging flux, both of which are very obvious in this event (Zhang et al. 2007; Kubo et al. 2007). The photospherically driven tether-cutting reconnection was discussed by Moore & Roumeliotis (1992). Chen & Shibata (2000) presented numerical simulations of CMEs and flares triggered by new emerging flux. We depict the reconnection process of the first step in Figure 8a. The feet of magnetic lines with opposite polarities are getting closer to each other because of the rotation of the sunspot or the emergence of new flux. Thus, the field lines reconnect when they touch each other. In fact, this early flare phase is similar to that described by Aschwanden et al. (1999), in which the connectivity of magnetic polarities is exchanged between the four loop footpoints. Wang & Shi (1993) suggested a two-step reconnection process, in which the first step takes place in the lower atmosphere. Recently, Moon et al. (2004) reported more observational evidence showing that magnetic reconnection in the lower atmosphere is related to filament eruptions and flares based on observations from MDI, TRACE, and Big Bear Solar Observatory. Some more evidence can also be found in Zhang et al. (2001), Kim et al. (2001), and Colman & Canfield (2001).

The reconnection in the lower atmosphere is key to triggering the whole two-ribbon flare. It starts the upward motion of the filament (e.g. Sterling et al. 2007). When the filament rises explosively, the envelope field is opened and stretched out, producing a current sheet below. Then, magnetic reconnection between en-

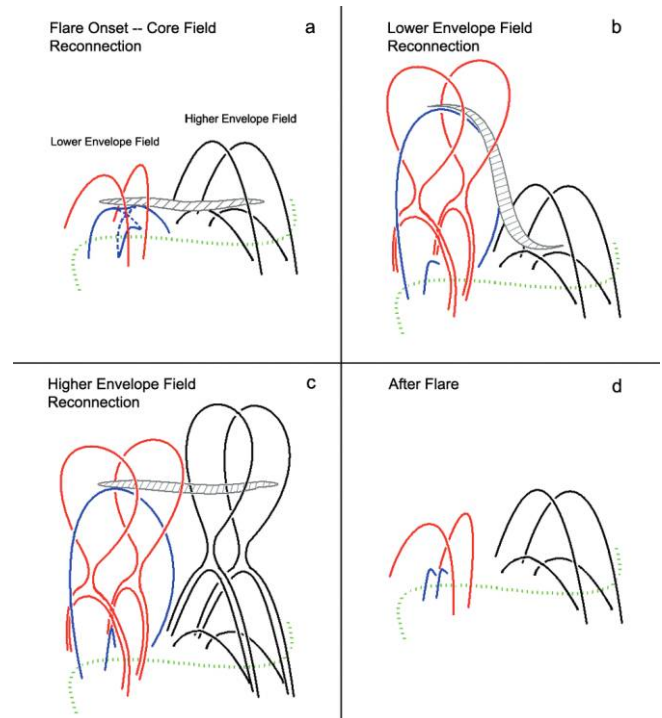


FIG. 8.— Sketch of the magnetic field configurations of the December 13 flare. The four panels represent four different stages of the flare. The green dashed line is the polarity inversion line. The hatched region refers to the filament passing through both the envelope fields. The blue dashed lines in panel a are core field lines before the reconnection, while the blue solid lines are lines after the reconnection. The lower envelope field reconnects first, and the higher one reconnects later. The core field becomes less sheared after the flare.

velope field lines occurs, which is the typical two-ribbon flare process. High-energy particles accelerated in the reconnection site precipitate along the field lines into the lower atmosphere, forming the two flare ribbons. In this process, the lower envelope field reconnects first, followed by the higher one, which is proved by the evolution of the ribbons. We show this process in Figures 8b–8c. The progressive reconnection is seen from the movie of the X-Ray Telescope (XRT) on board *Hinode*, which shows that the loops brighten gradually from the core field to the west. This process is shown from the activation of the filament, which rises first in the core field region and then extends to the west gradually.

The fact that the shear angle in a particular layer in the photosphere becomes larger after the flare than before the flare may provide more evidence in favor of the tether-cutting model. However, in general the core field becomes less sheared after the flare (Fig. 8d). On the other hand, reconnection of the envelope field forms a CME, which is observed by the Large Angle and Spectrometric Coronagraph on board the *Solar and Heliospheric Observatory* (SOHO LASCO). The relationship between the CME and the flare will be studied in our future work.

We are very grateful to the referee for helpful comments and to H. N. Wang for providing the code for removing the 180° ambiguity of the transverse field. *Hinode* is a Japanese mission developed and launched by ISAS/JAXA, collaborating with NAOJ as a domestic partner and NASA and STFC (UK) as international partners. Scientific operation of the *Hinode* mission is conducted by the *Hinode* science team organized at ISAS/JAXA. This team mainly consists of scientists from institutes in the partner countries.

Support for the postlaunch operation is provided by JAXA and NAOJ (Japan), STFC (UK), NASA, ESA, and NSC (Norway). *TRACE* was supported by contract NAS5-38099 from NASA to LMATC. Y. Guo and M. D. Ding were supported by the National

Natural Science Foundation of China (NSFC) under grants 10221001, 10333040, and 10673004 and by NKBRFS under grant 2006CB806302. T. Wiegmann was supported by DLR-grant 50 OC 0501.

REFERENCES

- Aly, J. J. 1989, *Sol. Phys.*, 120, 19
 Amari, T., Aly, J. J., Luciani, J. F., Boulmezaoud, T. Z., & Mikić, Z. 1997, *Sol. Phys.*, 174, 129
 Aschwanden, M. J., Kosugi, T., Hanaoka, Y., Nishio, M., & Melrose, D. B. 1999, *ApJ*, 526, 1026
 Berger, M. A. 1998, in *IAU Colloq. 167, New Perspectives on Solar Prominences*, ed. D. Webb, B. Schmieder, & D. Rust (San Francisco: ASP), 102
 Chen, P. F., & Shibata, K. 2000, *ApJ*, 545, 524
 Colman, A. M., & Canfield, R. C. 2001, *AGU Spring Meeting, Abs. SH22A-03*
 Handy, B. N., et al. 1999, *Sol. Phys.*, 187, 229
 Hirayama, T. 1974, *Sol. Phys.*, 34, 323
 Ichimoto, K., et al. 2008, *Sol. Phys.*, submitted
 Kim, J., Yun, H. S., Lee, S., Chae, J., Goode, P. R., & Wang, H. 2001, *ApJ*, 547, L85
 Kosugi, T., et al. 2007, *Sol. Phys.*, 243, 3
 Kubo, M., et al. 2007, *PASJ*, 59, S779
 Li, H., Sakurai, T., Ichimoto, K., & Ueno, S. 2000, *PASJ*, 52, 483
 Lites, B. W., Skumanich, A., Rees, D. E., & Murphy, G. A. 1988, *ApJ*, 330, 493
 Liu, C., Lee, J., Yurchyshyn, V., Deng, N., Cho, K., Karlichy, M., & Wang, H. 2007, *ApJ*, 669, 1372
 McClymont, A. N., Jiao, L., & Mikić, Z. 1997, *Sol. Phys.*, 174, 191
 Metcalf, T. R. 1994, *Sol. Phys.*, 155, 235
 Metcalf, T. R., et al. 2006, *Sol. Phys.*, 237, 267
 ———. 2008, *Sol. Phys.*, 247, 269
 Moon, Y.-J., Chae, J., Choe, G. S., Wang, H., Park, Y. D., & Cheng, C. Z. 2004, *J. Korean Astron. Soc.*, 37, 41
 Moore, R. L., & LaBonte, B. J. 1980, in *Solar and Interplanetary Dynamics*, ed. M. Dryer & E. Tandberg-Hanssen (Dordrecht: Reidel), 207
 Moore, R. L., & Roumeliotis, G. 1992, in *Eruptive Solar Flares*, ed. Z. Svestka, B. V. Jackson, & M. E. Machado (Berlin: Springer), 69
 Moore, R. L., Schmieder, B., Hathaway, D. H., & Tarbell, T. D. 1997, *Sol. Phys.*, 176, 153
 Moore, R. L., Sterling, A. C., Hudson, H. S., & Lemen, J. R. 2001, *ApJ*, 552, 833
 Régnier, S., Amari, T., & Kersalé, E. 2002, *A&A*, 392, 1119
 Rust, D. M., & Kumar, A. 1996, *ApJ*, 464, L199
 Scherrer, P. H., et al. 1995, *Sol. Phys.*, 162, 129
 Schrijver, C. J., DeRosa, M. L., Title, A. M., & Metcalf, T. R. 2005, *ApJ*, 628, 501
 Schrijver, C. J., et al. 2006, *Sol. Phys.*, 235, 161
 ———. 2008, *ApJ*, 675, 1637
 Shimizu, T., et al. 2008, *Sol. Phys.*, in press
 Sterling, A. C., & Hudson, H. S. 1997, *ApJ*, 491, L55
 Sterling, A. C., Moore, R. L., & *Hinode* team. 2007, *AAS Meeting*, 210, 72.07
 Stenflo, J. O. 1985, *Sol. Phys.*, 100, 189
 Suematsu, Y., et al. 2008, *Sol. Phys.*, in press
 Taylor, J. B. 1974, *Phys. Rev. Lett.*, 33, 1139
 ———. 1991, *Sol. Phys.*, 136, 37
 Tsuneta, S., et al. 2008, *Sol. Phys.*, in press
 Unno, W. 1956, *PASJ*, 8, 108
 Wang, H. 1997, *Sol. Phys.*, 174, 265
 Wang, H., Yan, Y., & Sakurai, T. 2001, *Sol. Phys.*, 201, 323
 Wang, J., & Shi, Z. 1993, *Sol. Phys.*, 143, 119
 Wheatland, M. S. 2006, *Sol. Phys.*, 238, 29
 ———. 2007, *Sol. Phys.*, 245, 251
 Wheatland, M. S., Sturrock, P. A., & Roumeliotis, G. 2000, *ApJ*, 540, 1150
 Wiegmann, T. 2004, *Sol. Phys.*, 219, 87
 ———. 2008, *J. Geophys. Res.*, 113, A03S02, doi:10.1029/2007JA012432
 Wiegmann, T., Inhester, B., Lagg, A., & Solanki, S. K. 2005a, *Sol. Phys.*, 228, 67
 Wiegmann, T., Inhester, B., & Sakurai, T. 2006, *Sol. Phys.*, 233, 215
 Wiegmann, T., Lagg, A., Solanki, S. K., Inhester, B., & Woch, J. 2005b, *A&A*, 433, 701
 Zhang, J., Li, L. P., & Song, Q. 2007, *ApJ*, 662, L35
 Zhang, J., Wang, J., Deng, Y., & Wu, D. 2001, *ApJ*, 548, L99